

PAIRING MECHANISM IN TWO HUBBARD MODELS THAT SHOW $d_{x^2-y^2}$ PAIRING

D.J. SCALAPINO

*Department of Physics, University of California, Santa Barbara,
CA 93106-9530, USA*

Here we examine various aspects of the pairing mechanism for two models, the two-dimensional and two-leg ladder Hubbard models. Both of these models exhibit pairing correlations with $d_{x^2-y^2}$ symmetry. However, the undoped insulating states of these two systems are different with the two-dimensional lattice characterized by a ground state with long-range antiferromagnetic order and the two-leg ladder having a spin gap in its ground state. Our aim is to gain a better understanding of the underlying pairing mechanism which causes $d_{x^2-y^2}$ pairing in these two models.

1 Introduction

Understanding the pairing mechanism responsible for superconductivity in the high-temperature superconducting cuprates remains one of the central issues in condensed matter physics. Various experiments [1,2,3] strongly suggest that the dominant symmetry of the gap in these materials is $d_{x^2-y^2}$. However, the implications of this for the pairing mechanism remain controversial [4]. In one view [5,6,7], antiferromagnetic spin-fluctuation exchange models provide a simple framework for understanding the $d_{x^2-y^2}$ symmetry of the gap. In addition, various phenomenological calculations based upon these ideas have often provided remarkable fits to data [2]. However, the effect of vertex corrections [8] as well as the unusual normal state properties and in particular the pseudogap phenomena [9] observed in the under-doped materials raise key questions which suggest that important pieces of the puzzle remain to be understood. Thus it seems useful to review what is understood about systems which show $d_{x^2-y^2}$ pairing fluctuations. Specifically, we propose to review some results which have been obtained for the two-dimensional Hubbard model and the two-leg Hubbard ladder. While it is not known whether the doped two-dimensional Hubbard model has a low-temperature superconducting phase, there is numerical evidence for $d_{x^2-y^2}$ pairing fluctuations in this model [5,10,11]. For the doped two-leg ladder, groundstate calculations [12] clearly show the presence of $d_{x^2-y^2}$ -like pairs. Furthermore, the undoped insulating states for these two systems are different. The ground state of the two-dimensional Hubbard model has long-range antiferromagnetic order [13], while that of the two-leg Hubbard ladder is characterized by a spin gap [12]. Both, however, have strong short-range antiferromagnetic correlations. Thus it is of interest to compare them and here we will examine these two cases with the aim of gaining insight into the mechanism underlying the tendency towards $d_{x^2-y^2}$ pairing in these systems.

After a summary of the energy scales which arise in the Hubbard model, we first turn to a discussion of the two-dimensional Hubbard model. Here we note the development of short-range antiferromagnetic correlations in the doped two-dimensional Hubbard model as the temperature is lowered below the exchange interaction $4t^2/U$. We examine the effect of these correlations on the structure of the quasiparticle spectrum and the effective particle-particle interaction. We then discuss how this interaction leads to a tendency towards $d_{x^2-y^2}$ pairing.

Following this, we turn to the example of the two-leg Hubbard ladder. Here we first discuss the half-filled insulating case, distinguishing between a band insulator and a strongly correlated spin gap insulator. Then we study the case of a doped ladder and discuss the nature of the observed pairing correlations.

The Hubbard model provides a simple model of the CuO₂ system:

$$H = -t \sum_{\langle ij \rangle, s} \left(c_{is}^\dagger c_{js} + c_{js}^\dagger c_{is} \right) + U \sum_i n_{i\uparrow} n_{i\downarrow}. \quad (1)$$

Here c_{is}^\dagger creates an electron of spin s on site i , in the first term the sum is over near-neighbor sites, and $n_{is} = c_{is}^\dagger c_{is}$ is the occupation number for electrons with spin s on site i . The one-electron transfer between near-neighbor sites is t , and U is an onsite Coulomb energy. In Eq. (1), we have chosen to keep only a near-neighbor hopping, but one could of course also add a next-near-neighbor hopping t' .

The bare energy scale is set by the bandwidth $8t$ and the effective Coulomb interaction U , which are both of order several electron volts. Near half-filling, electrons on neighboring sites tend to align antiferromagnetically so as to lower their energy by the exchange interaction $J = 4t^2/U$. This interaction is of order a tenth of an electron volt and, as we will see, sets the energy, or temperature scale, below which antiferromagnetic correlations, the low-energy structure in the single-particle spectral weight, and the pairing interaction develop.

While Monte Carlo [14] and Lanczos calculations [15] for a 4×4 lattice find that two holes added to the half-filled Hubbard ground state form a $d_{x^2-y^2}$ bound state, and density matrix renormalization group calculations [12] find that $d_{x^2-y^2}$ -like pairs are formed on two-leg Hubbard ladders, it is not known what happens for the two-dimensional Hubbard model. It is possible that on an energy scale of order $J/10$, a $d_{x^2-y^2}$ superconducting state forms. However, this may well require modifications of the model, such as an additional near-neighbor $\Delta J \mathbf{S}_i \cdot \mathbf{S}_j$ term or possibly a next-near-neighbor hopping t' . Nevertheless, it is known that as the temperature is reduced below J , $d_{x^2-y^2}$ pairing correlations develop in the doped two-dimensional Hubbard model, and here we will examine why this happens.

2 Two-Dimensional Hubbard Lattice

At half-filling, $\langle n_{i\uparrow} + n_{i\downarrow} \rangle = 1$, the 2D Hubbard model develops long-range antiferromagnetic order as the temperature goes to zero [13]. In the doped case, strong short-range antiferromagnetic correlations develop as the temperature decreases below J . This is clearly seen in the temperature dependence of the wave vector and Matsubara frequency-dependent magnetic susceptibility

$$\chi(\mathbf{q}, i\omega_m) = \frac{1}{N} \sum_{\ell} \int_0^\beta d\tau e^{i\omega_m \tau} e^{-i\mathbf{q} \cdot \ell} \langle m_{i+\ell}^-(\tau) m_i^+(0) \rangle. \quad (2)$$

Here $m_i^+(0) = c_{i\uparrow}^\dagger c_{i\downarrow}$ and $m_{i+\ell}^-(\tau) = e^{H\tau} m_{i+\ell}^-(0) e^{-H\tau}$, where $m_{i+\ell}^-(0)$ is the hermitian conjugate of $m_{i+\ell}^+(0)$. Monte Carlo results for $\chi(\mathbf{q}, 0)$ versus \mathbf{q} along the $(1, 1)$ axis for an 8×8 lattice with $U/t = 4$ and a filling $\langle n \rangle = 0.875$ are shown in Fig. 1(a). In Fig. 1(b), the Matsubara frequency dependence of $\chi(\mathbf{q}, i\omega_m)$ versus $\omega_m = 2\pi T$ is shown for $\mathbf{q} = (\pi, \pi)$. The inset of Fig. 1(b) shows the temperature dependence of the antiferromagnetic correlation length ξ . Here, ξ^{-1} is defined as the half-width at half-maximum of $\chi(\mathbf{q}, 0)$. The low-frequency nature of the antiferromagnetic correlations are seen in Fig. 2(a) where $\text{Im } \chi(\mathbf{q} = (\pi, \pi), \omega)$ versus ω is plotted at various temperatures. In addition, Fig. 2(b) shows $\text{Im } \chi(\mathbf{q}, \omega_Z)/\omega_Z$ versus \mathbf{q} in the $\omega_Z \rightarrow 0$ limit. This is the quantity which determines the NMR T_1^{-1} response of the system. These figures clearly show the development of significant short-range and low-frequency antiferromagnetic correlations as the temperature decreases below $J \simeq 4t^2/U$.

As these antiferromagnetic correlations develop, the single-particle spectral weight

$$A(\mathbf{p}, \omega) = -\frac{1}{\pi} \text{Im } G(\mathbf{p}, i\omega_n \rightarrow \omega + i\delta) \quad (3)$$

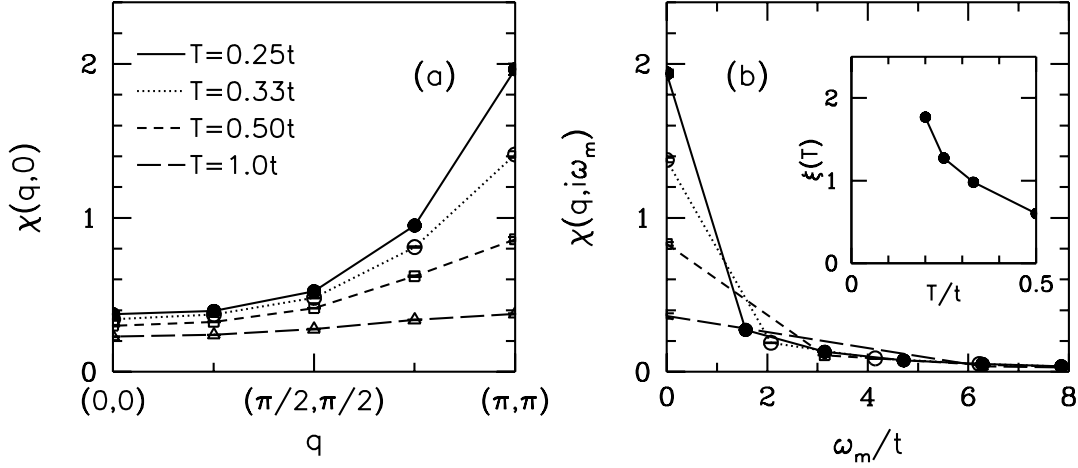


Figure 1: (a) Magnetic susceptibility $\chi(\mathbf{q}, 0)$ versus \mathbf{q} along the $(1,1)$ direction for various temperatures. These results are for an 8×8 lattice with $U/t = 4$ and a filling $\langle n \rangle = 0.875$. (b) Matsubara frequency dependence of $\chi(\mathbf{q}, i\omega_m)$ for $\mathbf{q} = (\pi, \pi)$ at the same temperatures as in Fig. 1(a). Note that as T decreases below $4t^2/U$, short-range antiferromagnetic fluctuations develop. Inset: Temperature dependence of the antiferromagnetic correlation length ξ .

and the density of states

$$N(\omega) = \frac{1}{N} \sum_{\mathbf{p}} A(\mathbf{p}, \omega) \quad (4)$$

also change. Figure 3(a) shows the temperature evolution of $N(\omega)$ for $U/t = 8$ and $\langle n \rangle = 0.875$. Figure 3(b) shows $N(\omega)$ for $U/t = 12$ and $T = 0.5t$. As the temperature is lowered, a peak appears on the upper edge of the lower Hubbard band. This peak arises from a narrow quasiparticle band shown in the single-particle spectral weight $A(\mathbf{p}, \omega)$ of Fig. 4 and plotted as the solid curve in Fig. 5. As the momentum \mathbf{p} goes towards the Γ point $(0,0)$, we believe that the quasiparticle peak is obscured by the lower Hubbard band because of the resolution of the maximum entropy technique which we have used. Indeed, at the Γ point a separate quasiparticle peak is found from Lanczos exact diagonalization [16] on a 4×4 lattice. The solid line in Fig. 5 shows what we believe is the quasiparticle dispersion relation. As clearly evident in the spectral weight shown in Figs. 4(a) and (b), the quasiparticle dispersion is anomalously flat near the $(\pi, 0)$ corner. As discussed by various authors [17,18], this reflects the influence of the antiferromagnetic correlations on the quasiparticle excitation energy. It is clear that the peak structure in $N(\omega)$ also arises from the short-range antiferromagnetic correlations and is a many-body effect rather than simply a non-interacting band Van Hove singularity.

Monte Carlo calculations have also been used to determine the two-fermion scattering vertex $\Gamma(p_1, p_2, p_3, p_4)$. Here p_1 stands for $(\mathbf{p}_1, i\omega_{n_1})$ and σ . Using Γ and the single-particle Green's function $G(p)$, one can solve the t -matrix equations shown diagrammatically in Fig. 6 to obtain the irreducible particle-hole and particle-particle vertices. The singlet irreducible particle-particle vertex $\Gamma_{\text{IS}}(p', -p', p, -p)$ in the zero center-of-mass momentum and energy channel represents the effective pairing interaction. In Fig. 7(a), $\Gamma_{\text{IS}}(q = p - p')$ is plotted for \mathbf{q} along the $(1,1)$ direction and $i\omega_n = i\omega_{n'} = i\pi T$, corresponding to zero Matsubara energy transfer. The Matsubara frequency dependence of this vertex for energy transfer $\omega_m = \omega_{n'} - \omega_n$ is shown in Fig. 7(b)

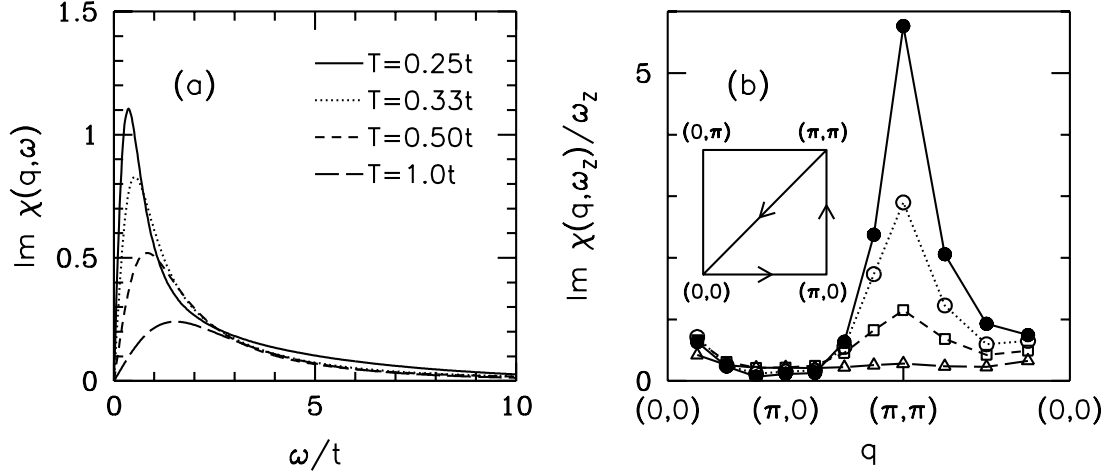


Figure 2: (a) Spin-fluctuation spectral weight $\text{Im } \chi(\mathbf{q}, \omega)$ versus ω at $\mathbf{q} = (\pi, \pi)$ for various temperatures. (b) $\text{Im } \chi(\mathbf{q}, \omega_z)/\omega_z$ versus \mathbf{q} in the limit of $\omega_z \rightarrow 0$ for the same temperatures as in Fig. 2(a). Here \mathbf{q} is plotted along the path shown in the inset. These figures are for $U/t = 4$ and $\langle n \rangle = 0.875$.

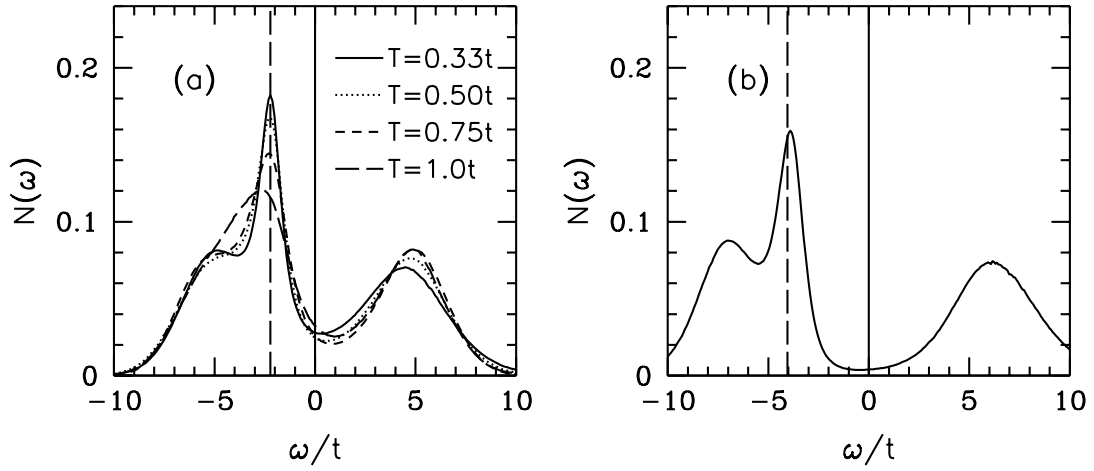


Figure 3: (a) Evolution of the single-particle density of states $N(\omega)$ with temperature for $U/t = 8$ and $\langle n \rangle = 0.875$. (b) $N(\omega)$ versus ω for $U/t = 12$, $\langle n \rangle = 0.875$ and $T = 0.5t$. The vertical dashed lines denote the chemical potential.

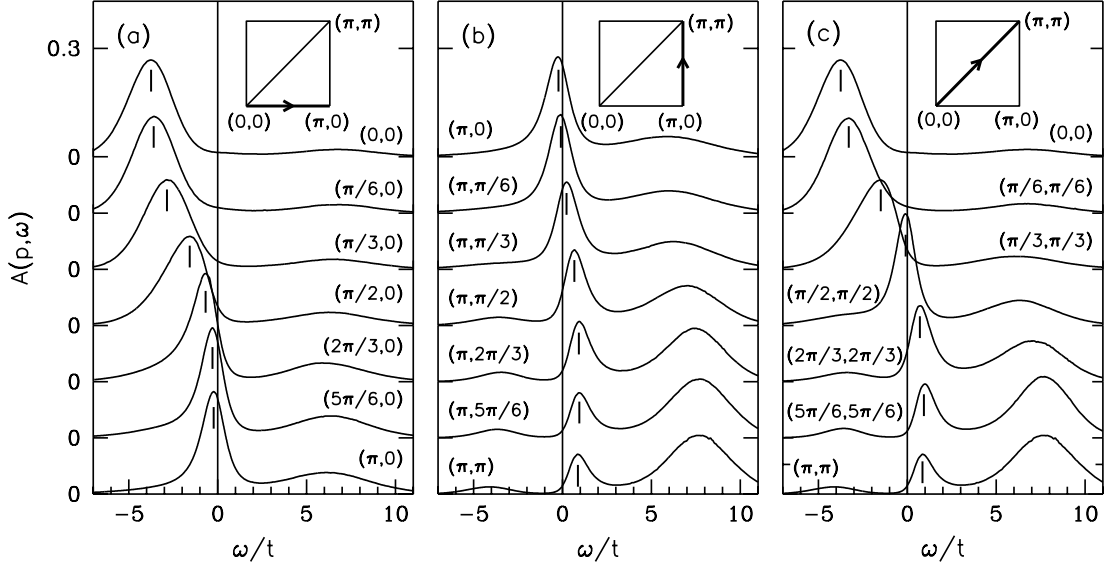


Figure 4: Single-particle spectral weight along various cuts in the Brillouin zone is shown for $U/t = 8$ and $\langle n \rangle = 0.875$ on a 12×12 lattice at $T = 0.5t$.

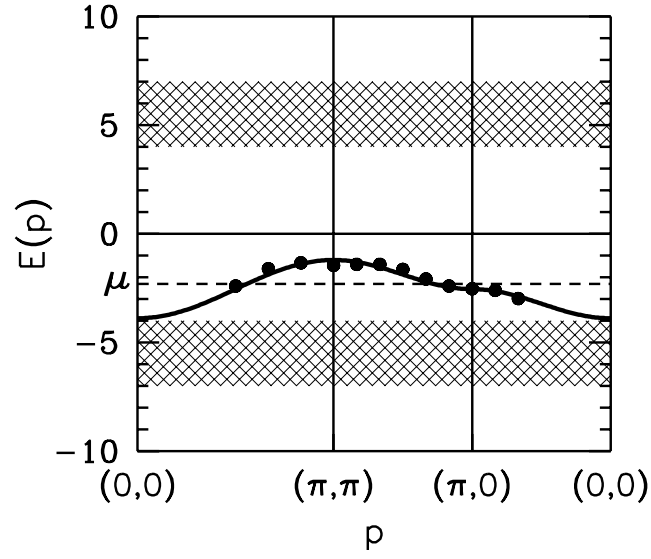


Figure 5: Dispersion of the quasiparticle peak in the spectral weight versus \mathbf{p} for $U/t = 8$, $\langle n \rangle = 0.875$ and $T = 0.5t$. The solid points mark the low-energy peaks of $A(\mathbf{p}, \omega)$ shown in Fig. 4, and the solid curve represents an estimate of the quasiparticle dispersion using these data and Lanczos results for \mathbf{p} near $(0,0)$. The broad darkened areas represent the incoherent spectral weight in the upper and lower Hubbard bands. The horizontal dashed line denotes the chemical potential μ .

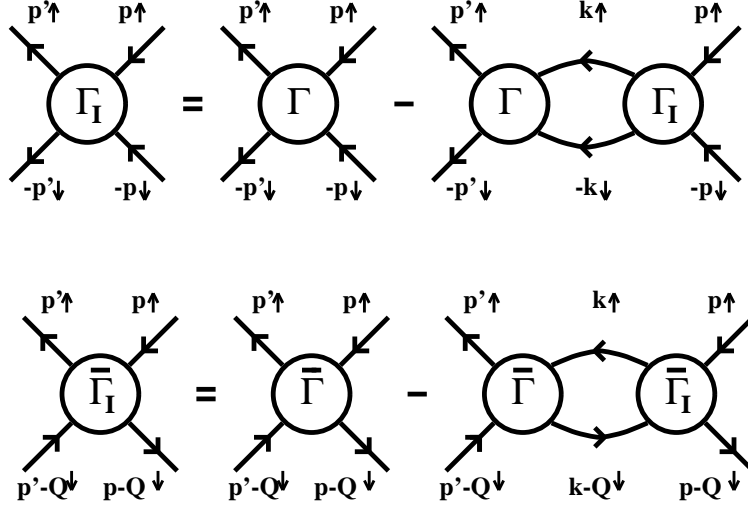


Figure 6: Particle-particle and particle-hole t -matrix equations.

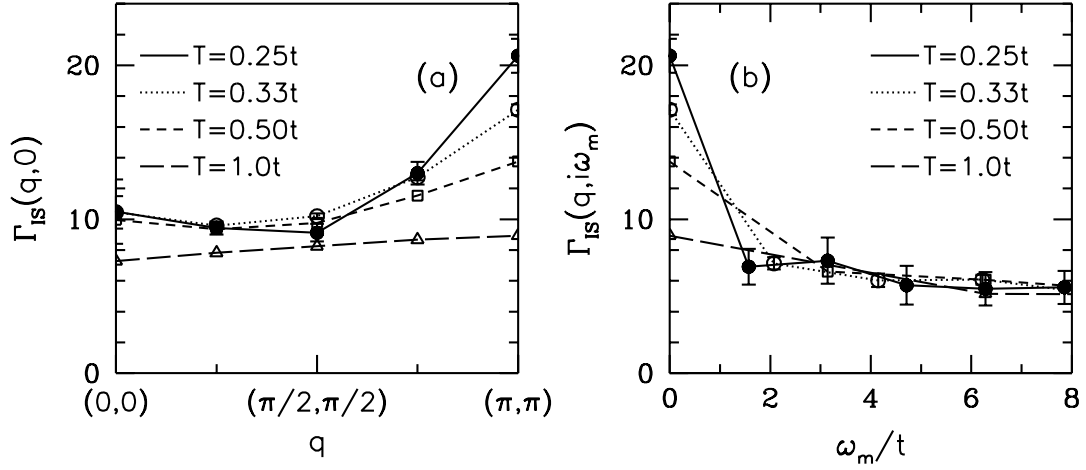


Figure 7: (a) Singlet irreducible particle-particle vertex for zero energy transfer $\Gamma_{\text{IS}}(\mathbf{q}, i\omega_m = 0)$ versus \mathbf{q} along the (1,1) direction. Here $U/t = 4$ and $\langle n \rangle = 0.875$. As the temperature decreases below $J = 4t^2/U$, the strength of the interaction is enhanced at large momentum transfer. (b) Energy transfer dependence of $\Gamma_{\text{IS}}(\mathbf{q}, i\omega_m)$ for $\mathbf{q} = (\pi, \pi)$, $\omega_n = \pi T$, and $\omega_{n'} = \omega_n + \omega_m$ is shown for various temperatures. Again note the similarity to $\chi(\mathbf{q}, i\omega_m)$ in Fig. 1.

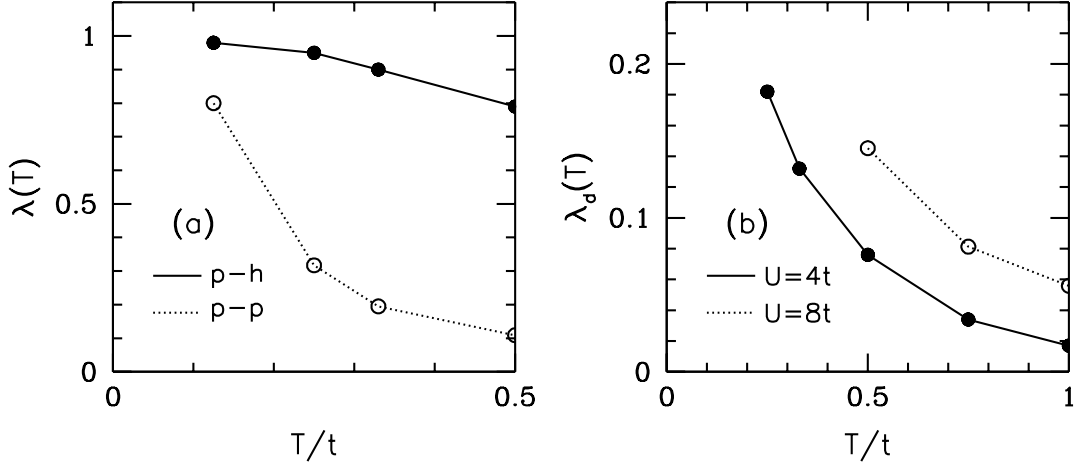


Figure 8: (a) Leading $\mathbf{Q} = (\pi, \pi)$, $S = 1$ particle-hole (solid circle) and the $\mathbf{Q} = 0$, singlet particle-particle (open circle) eigenvalues versus temperature for $U/t = 4$ and $\langle n \rangle = 1$. (b) Singlet $d_{x^2-y^2}$ eigenvalue versus temperature for $U/t = 4$ (solid circle) and $U/t = 8$ (open circle) at $\langle n \rangle = 0.875$.

for $\mathbf{q} = (\pi, \pi)$. Comparing Figs. 1 and 7, one clearly sees that the \mathbf{q} and ω_m structure of the interaction and $\chi(\mathbf{q}, i\omega_m)$ are similar, both reflecting the development of the antiferromagnetic correlations as T is reduced below J .

Given the Monte Carlo results for the irreducible particle-particle vertex $\Gamma_{\text{IS}}(p', -p', p, -p)$ in the zero energy and center-of-mass momentum channel, which we will denote by $\Gamma_{\text{IS}}(p'|p)$ and the single-particle Green's function $G_\sigma(p)$, the Bethe-Salpeter equation for the particle-particle channel is

$$\lambda_\alpha \phi_\alpha(p) = -\frac{T}{N} \sum_{p'} \Gamma_{\text{IS}}(p|p') G_\uparrow(p') G_\downarrow(-p') \phi_\alpha(p'). \quad (5)$$

Here, as before, the sum on p' is over both \mathbf{p}' and $\omega_{n'} = (2n' + 1)\pi T$. Using the same Monte Carlo data for the four-point vertex, one can also determine the irreducible particle-hole vertex $\bar{\Gamma}_{\text{I}}(p|p')$ for a center-of-mass momentum $\mathbf{Q} = (\pi, \pi)$ and spin 1. Then, using this as a kernel, the Bethe-Salpeter equation for the $\mathbf{Q} = (\pi, \pi)$ particle-hole channel is

$$\bar{\lambda}_\alpha \bar{\phi}_\alpha(p) = -\frac{T}{N} \sum_{p'} \bar{\Gamma}_{\text{I}}(p|p') G_\uparrow(p' + Q) G_\downarrow(p') \bar{\phi}_\alpha(p'). \quad (6)$$

Results showing the temperature dependence of the leading even frequency eigenvalues for the particle-particle ($\mathbf{Q} = 0$) and particle-hole ($\mathbf{Q} = (\pi, \pi)$) channels for a half-filled 8×8 lattice with $U/t = 4$ are plotted in Fig. 8(a). At half-filling, the dominant eigenvalue occurs in the particle-hole $\mathbf{Q} = (\pi, \pi)$ spin $S = 1$ channel, reflecting the development of long-range antiferromagnetic correlations in the half-filled ground state. The $\mathbf{Q} = (\pi, \pi)$ magnetic susceptibility varies as

$$\chi(T) \sim (1 - \bar{\lambda}(T))^{-1} \quad (7)$$

and diverges as T goes to zero. The leading even frequency singlet particle-particle eigenvalue is associated with an eigenfunction $\phi(\mathbf{p}, i\omega_n)$ which has $d_{x^2-y^2}$ symmetry as shown in Fig. 9.

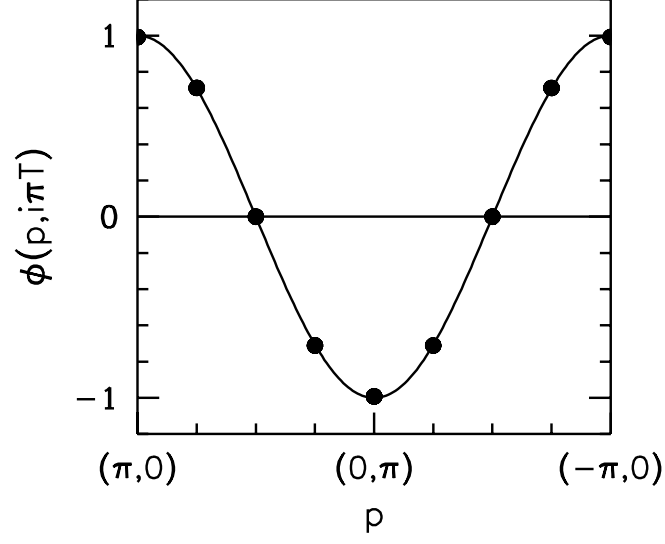


Figure 9: Momentum dependence of the leading singlet even-frequency particle-particle eigenfunction $\phi(\mathbf{p}, i\omega_n)$ at $\omega_n = \pi T$ for $U/t = 4$, $\langle n \rangle = 0.875$ and $T = 0.25t$. Here, \mathbf{p} moves on the Fermi surface of the half-filled noninteracting system from $(\pi, 0)$ to $(-\pi, 0)$, and $\phi(\mathbf{p}, i\pi T)$ has been normalized by its value at $\mathbf{p} = (\pi, 0)$. The solid line denotes $(\cos p_x - \cos p_y)/2$. Hence, near the Fermi surface $\phi(\mathbf{p}, i\pi T)$ is very close to the $(\cos p_x - \cos p_y)/2$ form.

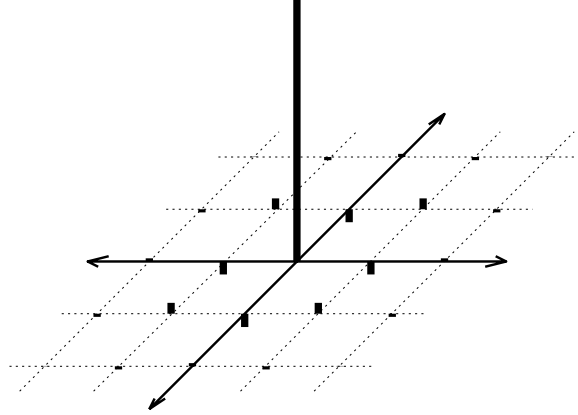


Figure 10: Real space structure of $\Gamma_{IS}(\ell)$ for $U/t = 4$, $\langle n \rangle = 0.875$ and $T = 0.25t$.

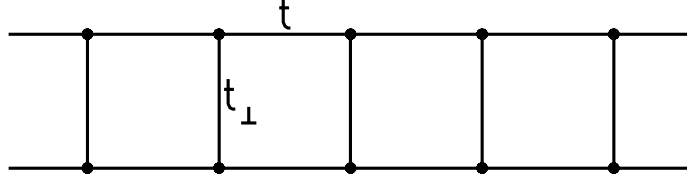


Figure 11: Two-chain Hubbard lattice with inter-chain and intra-chain hopping matrix elements t_{\perp} and t , respectively.

Its rapid increase at low temperature reflects the fact that the doped two-hole (or two-particle) state is bound [14,15].

For $\langle n \rangle = 0.875$, the Monte Carlo calculations are limited to higher temperatures because of the fermion determinantal sign problem. However, as seen in Fig. 8(b) for $U/t = 4$ and 8, the $d_{x^2-y^2}$ eigenvalue increases as the temperature is lowered. This is associated with the development of short range antiferromagnetic correlations and the increase in Γ_{IS} at large momentum transfer. In this context it is interesting to plot the real space Fourier transform

$$\Gamma_{\text{IS}}(\ell) = \frac{1}{N} \sum_{\mathbf{q}} e^{i\mathbf{q} \cdot \ell} \Gamma_{\text{IS}}(\mathbf{q}, i\omega_m = 0) \quad (8)$$

As seen in Fig. 10, $\Gamma_{\text{IS}}(\ell)$ is repulsive on site but attractive on near neighbor sites. It is this feature along with the large Fermi surface that leads to the $d_{x^2-y^2}$ pairing fluctuations in the two-dimensional Hubbard model.

3 Ladders

New materials consisting of arrays of weakly coupled Cu-O ladders have recently been synthesized [19]. These systems provide further opportunities to examine the physical properties of strongly correlated insulators and the metallic state which is reached when holes are doped into such insulators. Here we present a short review of the results which have been obtained for the two-chain Hubbard ladder using a numerical density matrix renormalization group (DMRG) method [12].

The two-chain Cu-O ladders in SrCuO_3 and $\text{La}_2\text{Cu}_2\text{O}_5$ consist of Cu-O-Cu legs joined by placing an O atom between the Cu atoms of the legs, forming Cu-O-Cu rungs. In both cases, the ladders are also coupled to each other, but here we consider the idealized case of an isolated ladder. Furthermore, we approximate the ladder by the two-chain Hubbard lattice shown in Fig. 11. Here

$$H = -t \sum_{i,\lambda,\sigma} \left(c_{i,\lambda,\sigma}^{\dagger} c_{i+1,\lambda,\sigma} + c_{i+1,\lambda,\sigma}^{\dagger} c_{i,\lambda,\sigma} \right) - t_{\perp} \sum_{i,\sigma} \left(c_{i,1\sigma}^{\dagger} c_{i,2\sigma} + c_{i,2\sigma}^{\dagger} c_{i,1\sigma} \right) + U \sum_{i,\lambda} n_{i,\lambda\uparrow} n_{i,\lambda\downarrow} \quad (9)$$

with t the hopping integral parallel to the chains, t_{\perp} the hopping between the legs, and U the onsite Coulomb interaction. The operator $c_{i,\lambda s}^{\dagger}$ creates an electron of spin s on site (i, λ) with $\lambda = 1, 2$ denoting the leg and $n_{i,\lambda s} = c_{i,\lambda s}^{\dagger} c_{i,\lambda s}$. For $U = 0$, H can be diagonalized in terms

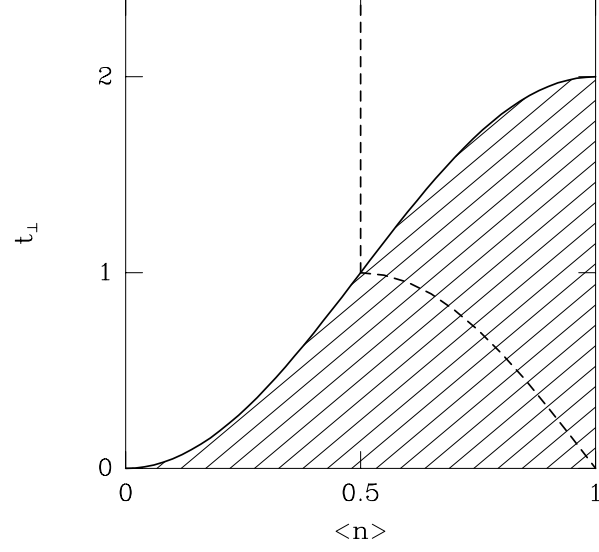


Figure 12: Phase diagram of the $U = 0$ system.

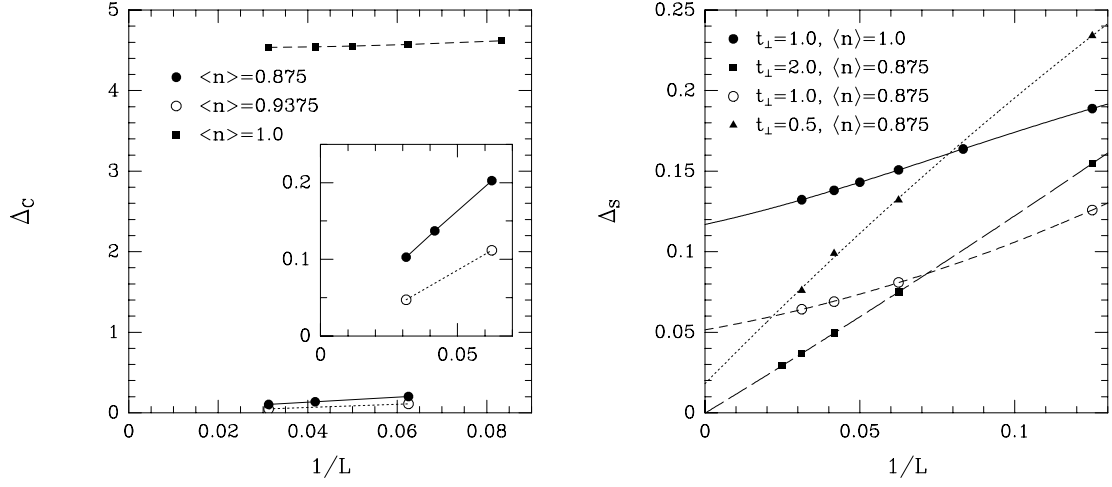


Figure 13: (a) Charge and (b) spin gaps, Δ_c and Δ_s , versus the inverse lattice length L^{-1} for $U/t = 8$.

of bonding ($-$) and antibonding ($+$) bands with $\varepsilon_k = 2t \cos k_x \pm t_\perp$. A phase diagram for the two-chain ladder is sketched in Fig. 12 for $U = 0$. The region above the line $t_\perp/t = 1 - \cos(\pi\langle n \rangle)$, with $\langle n \rangle = \langle n_{i\uparrow} + n_{i\downarrow} \rangle$ the site filling, corresponds to having electrons only occupy the bonding band. The shaded region has both the bonding and antibonding band occupied with the bonding band half-occupied along the dashed curve. Thus for the half-filled case, $\langle n \rangle = 1$, the bonding band is full when t_\perp/t exceeds 2 and the non-interacting system is a simple band insulator with equal charge and spin gaps set by $2(t_\perp - 2t)$. In the non-interacting $U = 0$ limit, for t_\perp/t less than 2, electrons occupy both bands and the system behaves as a simple metal with vanishing charge and spin gaps. Here we will see that the situation is quite different in the presence of the Coulomb interaction U . At half-filling with $U \neq 0$, the system remains an insulator for $t_\perp/t < 2$, with a ratio of the spin gap to charge gap which approaches zero smoothly as t_\perp/t vanishes. Furthermore, holes doped into this correlated insulator form $d_{x^2-y^2}$ -like pairs which exhibit power-law correlations over much of the shaded region, and while the charge-gap vanishes, a finite spin gap remains.

The charge and spin gaps can be determined from the ground state energy $E_0(N_\uparrow, N_\downarrow)$ of a configuration with N_\uparrow up-spin and N_\downarrow down-spin electrons. The charge gap Δ_c is

$$\Delta_c = \frac{1}{2} [E_0(N_\uparrow + 1, N_\downarrow + 1) - E_0(N_\uparrow, N_\downarrow)], \quad (10)$$

and the spin gap

$$\Delta_s = E_0(N_\uparrow + 1, N_\downarrow - 1) - E_0(N_\uparrow, N_\downarrow). \quad (11)$$

Here $N_\uparrow = N_\downarrow$ and $N_\uparrow + N_\downarrow$ is fixed to give the desired filling $\langle n \rangle = (N_\uparrow + N_\downarrow)/L$ for a $2 \times L$ site ladder. Using the DMRG, calculations on ladders of varying lengths ($2 \times L$) have been carried out, giving the $L \rightarrow \infty$ extrapolations for Δ_c and Δ_s shown in Fig. 13 for $U/t = 8$ and various fillings. In this way, one finds that Δ_c and Δ_s are both finite for $\langle n \rangle = 1$ but Δ_c vanishes for $\langle n \rangle \neq 1$. A plot of Δ_s/Δ_c versus t_\perp/t for $\langle n \rangle = 1$ is shown in Fig. 14 for several values of U/t . For the interacting system Δ_s/Δ_c gradually approaches 1 as t_\perp/t increases beyond 2. The difference $(1 - \Delta_s/\Delta_c)$ is one characteristic difference between the strongly correlated insulating state and the band insulating state.

As noted, when holes are doped into the half-filled ladder, the charge gap vanishes. However, a spin gap remains which for a fixed value of U/t depends upon the ratio of t_\perp/t and the filling. In the following discussion, we will set $U/t = 8$ and $\langle n \rangle = 0.875$, and examine the properties of the system for various values of t_\perp/t . The dependence of the spin gap on t_\perp/t is illustrated in Fig. 15. For $t_\perp/t \gtrsim 1.7$, the spin gap vanishes, consistent with the one-band Luttinger liquid picture suggested by Fig. 12. For $U = 0$, the anti-bonding band becomes empty for $\langle n \rangle = 0.875$ when t_\perp/t exceeds 1.85. As t_\perp/t decreases, the spin gap rises and then appears to vanish for $t_\perp/t \simeq 0.43$. This is near the point at which the bonding band is half-filled, and as discussed by Balents and Fisher [20], a RNG calculation finds that the spin gap vanishes. At still lower values of t_\perp/t , the RNG calculation finds a small spin gap, but we have been unable to resolve it if it is indeed present.

In the spin gap regime of the doped system, the dominant two-particle correlations appear in the pairing channel. Figure 16 shows the rung-rung and rung-leg pair-field correlation functions

$$D_{xx}(\ell) = \langle \Delta_x(i + \ell) \Delta_x^\dagger(i) \rangle \quad (12)$$

and

$$D_{yx}(\ell) = \langle \Delta_y(i + \ell) \Delta_x^\dagger(i) \rangle. \quad (13)$$

Here

$$\Delta_x^\dagger(i) = \left(c_{1i\uparrow}^\dagger c_{2i\downarrow}^\dagger - c_{1i\downarrow}^\dagger c_{2i\uparrow}^\dagger \right) \quad (14)$$

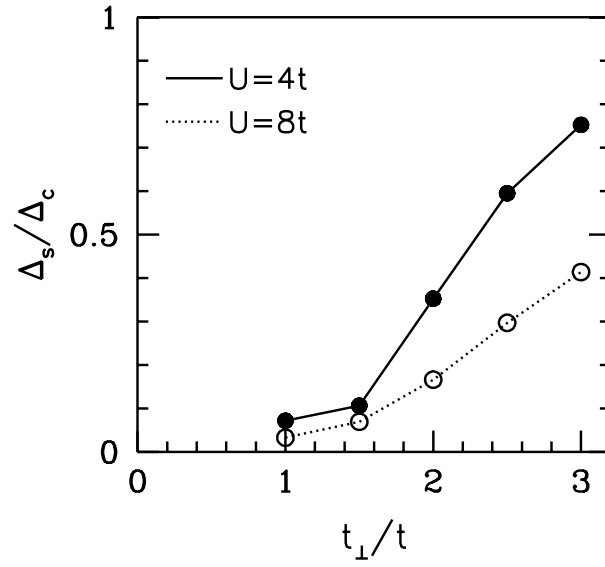


Figure 14: Ratio of the spin and charge gaps, Δ_s/Δ_c , versus t_{\perp}/t for $U/t = 4$ and 8 at $\langle n \rangle = 0.875$.

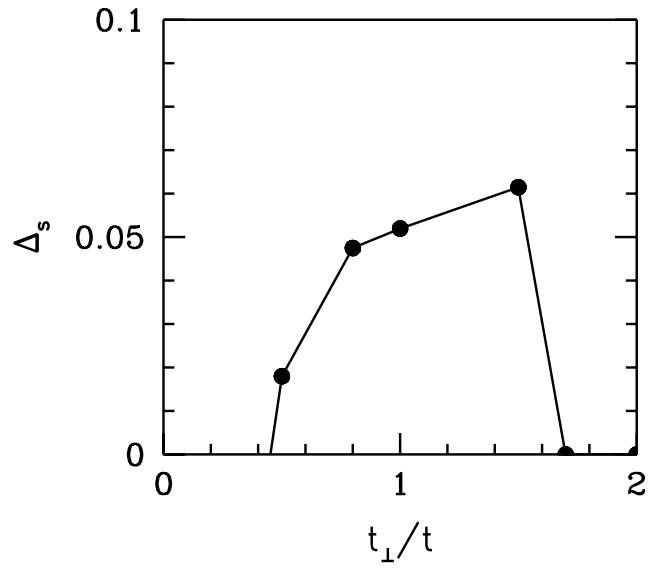


Figure 15: Spin gap Δ_s versus t_{\perp}/t for $U/t = 8$ and $\langle n \rangle = 0.875$.

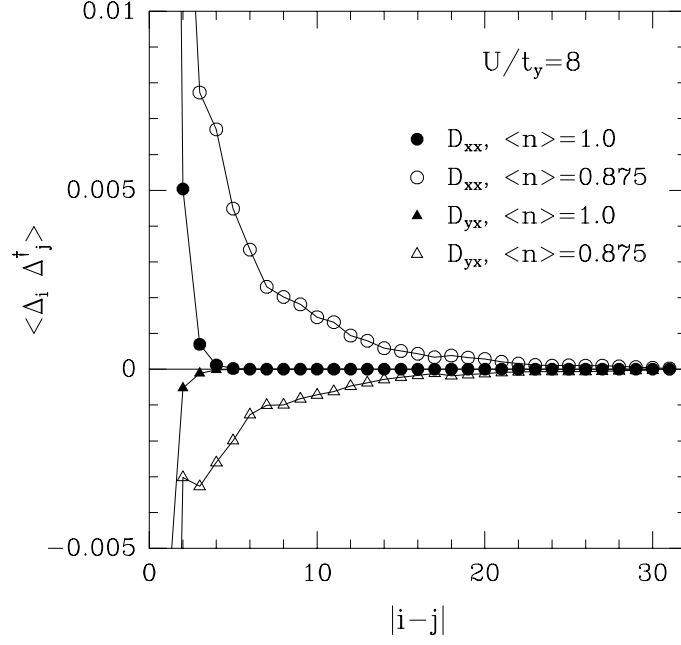


Figure 16: Pair field correlation functions $D_{xx}(\ell)$ and $D_{yx}(\ell)$ versus the lattice spacing $\ell = |i - j|$.

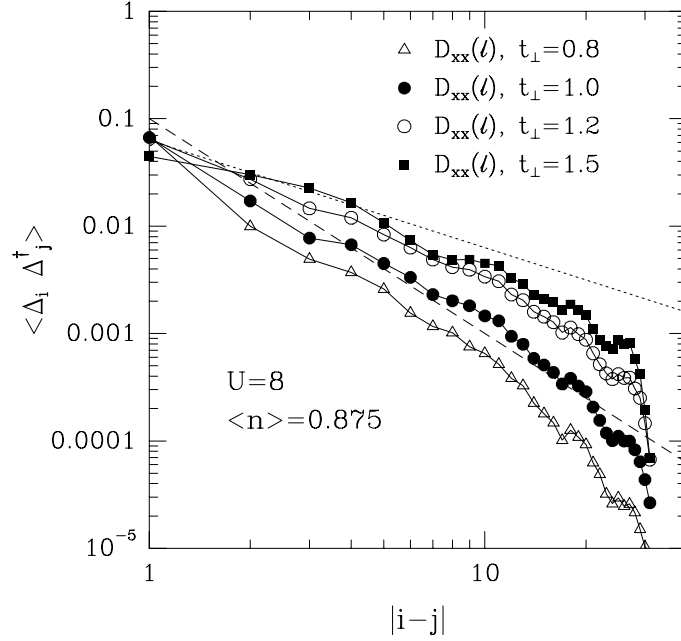


Figure 17: Power law decay of $D_{xx}(\ell = |i - j|)$ for different values of t_\perp/t at $U/t = 8$ and $\langle n \rangle = 0.875$. The dotted and the dashed lines decay as $|i - j|^{-1}$ and $|i - j|^{-2}$, respectively.

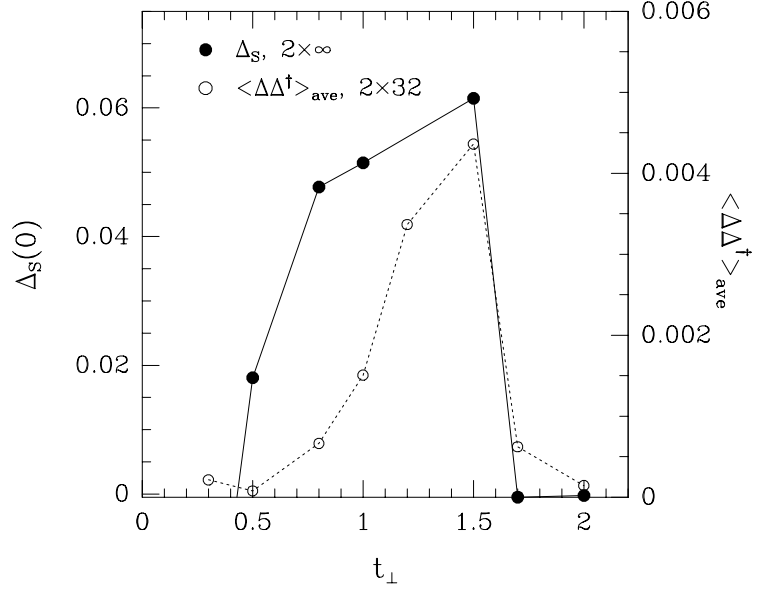


Figure 18: Comparison of the strength of the pairing correlations (open circle) with the size of the spin gap Δ_s (solid circle) for $U/t = 8$ and $\langle n \rangle = 0.875$. The average over ℓ of $\langle \Delta_i \Delta_{i+\ell} \rangle_{\text{ave}}$ has been done for ℓ between 8 and 12 lattice spacings.

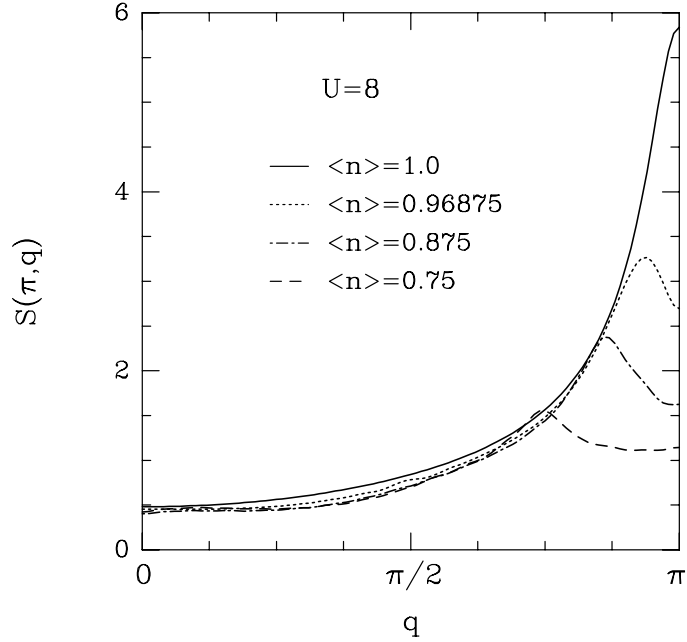


Figure 19: Magnetic structure factor $S(\pi, q)$ versus q along the ladder for $U/t = 8$ and various fillings.

creates a singlet pair on the i th rung, while

$$\Delta_y^\dagger(i) = \left(c_{1i\uparrow}^\dagger c_{1i+1\downarrow}^\dagger - c_{1i\downarrow}^\dagger c_{1i+1\uparrow}^\dagger \right) \quad (15)$$

creates a singlet pair along a leg of the ladder at site i . The Cu-O hopping parameters t and t_\perp have the same sign, so that the relative phases of the pair-field correlations shown in Fig. 16 are meaningful and imply that the bound pairs have $d_{x^2-y^2}$ -like symmetry, as discussed by Rice *et al.* [21] The power law decay of these pairing correlations is shown in Fig. 17. It is also interesting to compare the strength of the pairing correlations with the size of the spin gap. This is done in Fig. 18.

These results support a picture in which the doped state of the two-leg Hubbard ladder, in the appropriate t_\perp/t regime, is characterized by a finite spin gap and $d_{x^2-y^2}$ -like power-law pairing correlations. In Fig. 19, we show plots of the magnetic structure factor $S(\pi, q)$ with q along the ladder for various fillings. In the doped ladders, the peak in the structure factor occurs at an incommensurate wavevector. The exponential decay of the magnetization-magnetization correlation functions in the spin-gapped regime lead to Lorentzian line shapes. Thus even though the antiferromagnetic correlations are clearly short range, they lead to power law $d_{x^2-y^2}$ pairing correlations.

4 Conclusions

The development of both the low-energy quasiparticle dispersion and the peak in the singlet particle-particle vertex at large momentum transfers reflects the growth of the short-range antiferromagnetic correlations as T decreases below J . Analysis of the Bethe-Salpeter equation shows that the leading even-frequency singlet pairing occurs in the $d_{x^2-y^2}$ channel. Physically, for the large Fermi surface associated with the observed quasiparticle dispersion, a particle-particle vertex which increases at large momentum transfer favors $d_{x^2-y^2}$ pairing. Note that the tendency for $d_{x^2-y^2}$ pairing does not require a particularly sharp or narrow peak in $\Gamma_{\text{IS}}(p-p')$ for $\mathbf{p} - \mathbf{p}' = (\pi, \pi)$, but rather simply weight at large momentum transfers corresponding to strong short-range antiferromagnetic correlations. This is clearly seen in the results for the two-leg ladder where the antiferromagnetic correlations exponentially decay. Thus it is the strong short-range antiferromagnetic correlations which lead to the formation of $d_{x^2-y^2}$ pairing correlations in the Hubbard model.

Acknowledgments

The work on the 2D Hubbard model discussed here was carried out with N. Bulut and S.R. White. The work on the ladder was carried out with R. Noack and S.R. White. This work was supported in part by the National Science Foundation under grant No. DMR92-25027. The numerical computations reported in this paper were carried out at the San Diego Supercomputer Center.

References

1. J.R. Schrieffer, *Solid State Commun.* **92**, 129 (1995)
2. D.J. Scalapino, *Phys. Reports* **250**, 329 (1995).
3. D. Van Harlingen, *Rev. Mod. Phys.* **67**, 515 (1995).
4. D.J. Scalapino, *Physica C* **235-240**, 107 (1994).
5. N.E. Bickers, D.J. Scalapino and S.R. White, *Phys. Rev. Lett.* **62**, 961 (1989).

6. T. Moriya, Y. Takahashi and K. Ueda, *J. Phys. Soc. Japan* **59**, 2905 (1990).
7. P. Monthoux and D. Pines, *Phys. Rev. Lett.* **69**, 961 (1992).
8. J.R. Schrieffer, *J. Low Temp. Phys.* **99**, 397 (1995).
9. Proceedings of the *10th Anniversary HTS Workshop on Physics, Materials and Applications*, held in Houston, March 12-16, 1996.
10. N. Bulut, D.J. Scalapino and S.R. White, *Phys. Rev. B* **47**, 6157 (1993).
11. N. Bulut, D.J. Scalapino and S.R. White, *Phys. Rev. B* **50**, 9623 (1994).
12. R.M. Noack, S.R. White, and D.J. Scalapino, *Phys. Rev. Lett.* **73**, 882 (1994); R.M. Noack, S.R. White, and D.J. Scalapino, *Europhys. Lett.* **30**, 163 (1995).
13. J.E. Hirsch and S. Tang, *Phys. Rev. Lett.* **62**, 591 (1989).
14. E. Dagotto, A. Moreo, R.L. Sugar, and D. Toussaint, *Phys. Rev. B* **41**, 811 (1990).
15. A. Parola, S. Sorella, M. Parrinello, and E. Tosatti, *Phys. Rev. B* **43**, 6190 (1991).
16. E. Dagotto, A. Moreo, F. Ortolani, J. Riera, and D.J. Scalapino, *Phys. Rev. Lett.* **67**, 1918 (1991); E. Dagotto, F. Ortolani, and D.J. Scalapino, *Phys. Rev. B* **46**, 3183 (1992).
17. N. Bulut, D.J. Scalapino, and S.R. White, *Phys. Rev. B* **50**, 7215 (1994).
18. A. Moreo, S. Haas, A.W. Sandvik, and E. Dagotto, *Phys. Rev. B* **51**, 12045 (1995).
19. Z. Hirol and M. Takano, *Nature* **377**, 41 (1995).
20. L. Balents and M.P.A. Fisher, preprint.
21. T.M. Rice, M. Troyer, and H. Tsunetsugu, *J. Phys. Chem. Solids* **56**, 1663 (1995).